Boiling crisis as a critical phenomenon: Supplemental Material

I. KUTATELADZE DIMENSIONAL ANALYSIS AND EXPERIMENTAL DATA

According to the Kutateladze dimensional analysis [1], the critical heat flux Φ_C results from an interplay of three energetic scales:

- (i) the interfacial energy associated with bubble creation: $\sim \sigma R^2$ (where R is the typical bubble radius and σ the surface tension);
- (ii) the gravitational potential energy due to the buoyancy forces acting on gas bubbles: $\sim R^3(\rho_L - \rho_G)gR$ (with g - the acceleration of gravity and $\rho_L(_G)$ - the liquid (gas) density);
- (iii) the kinetic energy of the gas bubbles: $\sim \rho_G R^3 v^2$ (where v is the typical speed of bubble detachment from the hot surface).

Two scaling relations can be constructed: one describing bubble formation and another one describing bubble release, respectively:

$$\sigma R^2 \sim R^3(\rho_L - \rho_G)gR; \qquad R^3(\rho_L - \rho_G)gR \sim \rho_G R^3 v^2 \tag{1}$$

From these relations, one can obtain the typical size of the gas bubbles $R \sim \sqrt{\sigma/(g(\rho_L - \rho_G))}$ and the typical speed of the bubbles departure $v \sim \frac{1}{\sqrt{\rho_G}} \sqrt[4]{\sigma(\rho_L - \rho_G)g}$. From the knowledge of v we can obtain the scaling for the critical heat flux: $\Phi_C = L\rho_g v = XL\sqrt{\rho_G}\sqrt[4]{g\sigma(\rho_L - \rho_G)}$. The pre-factor X contains information about many neglected factors like surface roughness, flow geometry, wetting properties, etc. However, it is expected to preserve the order of magnitude of the predicted value of the Φ_C. In the past many attempts have been made to determine the value of X. Thus, Zuber [2] derived analytically the value $X = \pi/24 = 0.13$ for flat horizontal surfaces with perpendicular flow of the fluid. Other studies [1, 3, 4] have been aimed at correlating available experimental data and all of them rendered values around $X = 0.15$. The Kutateladze formula is now considered to be standard in the field.

If we now take into consideration the parameter values for N_2 at $T = 77$K (see table I), and use the Kutateladze formula for Φ_C with the pre-factor $X = 0.15$, the resulting value is $\Phi_C \simeq 14\text{W/cm}^2$. In turn, the temporal evolution of the heat flux $\Phi(t)$ in our experiments was obtained from the temperature evolution $T(t)$ of the aluminum sample (see Fig. 2 in the manuscript) by using the equation $\Phi(t) = C(t)dT(t)/dt$, where the heat capacity of Al $C(t)$ has been taken from the literature [5]. The Nukiyama curve (Heat flux Φ as a function of wall overheat $(T - T_t)/T_t$ where T_t is the saturation temperature of N_2) was also obtained from our experimental data and the knowledge of $C(t)$ (see inset in Fig. 2 in the manuscript). The maximum value of the heat flux renders $\max(\Phi(t)) \equiv \Phi_C = 2.5\text{W/cm}^2$, which is less than one order of magnitude lower than the Kutateladze estimation ($\Phi_C = 14\text{W/cm}^2$). Such a discrepancy is most probably a result of the geometric factors. Indeed, we recall that the value $X = 0.15$ corresponds to a flat horizontal surface with bubbles raising vertically while in our experiment we deal with an immersed cylinder having round, vertical surfaces.

C_G	741.5 J/kg K
C_L	2042 J/kg K
K_G	0.02583 J/m K s
K_L	0.1393 J/m K s
L	$1.991761 \cdot 10^5$ J/kg
T_t	77.36 K
ρ_G	4.61214 kg/m^3
ρ_L	806.084 kg/m^3
σ	0.00887484 Nm/m^2

TABLE I: Physical parameters for N_2 taken from [6], used in both the Kutateladze formula and the numerical simulations. C_G (C_L) is the heat capacity of the gas (liquid), K_G (K_L) is the thermal conductivity of the gas (liquid), L is the latent heat, T_t is the saturation temperature, ρ_G (ρ_L) is the gas (liquid) density and σ is the surface tension.

II. EXPERIMENTAL HISTOGRAMS AND REPRODUCIBILITY OF THE POWER-LAW BEHAVIOR

For the sake of clarity, in fig. 1 we show the energy histograms and the power spectrums of the different regimes in separated panels. The power-law slopes obtained in the energy histogram and the power spectrum at the crisis are also depicted in the film and nucleate boiling regimes to favor the comparison.

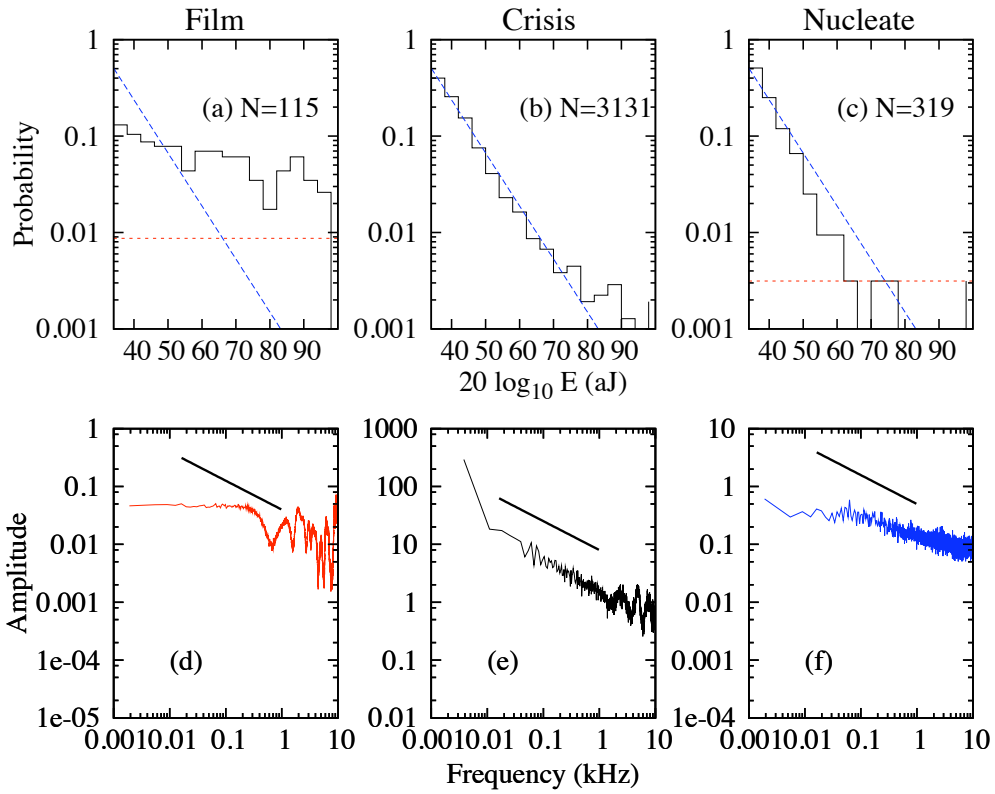

FIG. 1: Upper panels: Energy distribution associated with (a) film, (b) crisis and (c) nucleate boiling regimes. N indicates the number of AE events and the horizontal dashed lines indicate the level of one count. The diagonal line $p(E)dE \propto E^{-2.1}dE$ corresponds to the best-fit power-law probability density function in the crisis regime. Lower panels: Power spectrums calculated in (d) film, (e) crisis and (f) nucleate boiling regimes. The straight line $\sim 1/f^{0.5}$ corresponds to the fit in the crisis regime.

Regarding reproducibility of the results, in the paper we report data corresponding to three experiments (see the caption to Fig. 2 in the paper). In fact, many more experiments have been performed to eliminate the effects of the size of the vessel, the geometry of the sample and the material of the sample. In particular the size of the sample was varied tenfold and a range of metals have been tested without any effect on the critical exponent. Additional examples that we could not fit into the Letter format are shown in Fig. 2.

III. MODEL DETAILS

Our goal was to describe only the corresponding universality class which justifies some drastic simplifications. Several additional details of the algorithm are presented below. The main dimensionless equation takes the form

$$\frac{d\bar{T}}{d\bar{t}} + \frac{d\bar{\xi}}{d\bar{t}} = \frac{1}{\mathbf{Pe}}\Delta\bar{T}. \tag{2}$$

During fast advection steps it simplifies to

$$\frac{d\bar{T}}{d\bar{t}} + \frac{d\bar{\xi}}{d\bar{t}} = 0. \tag{3}$$

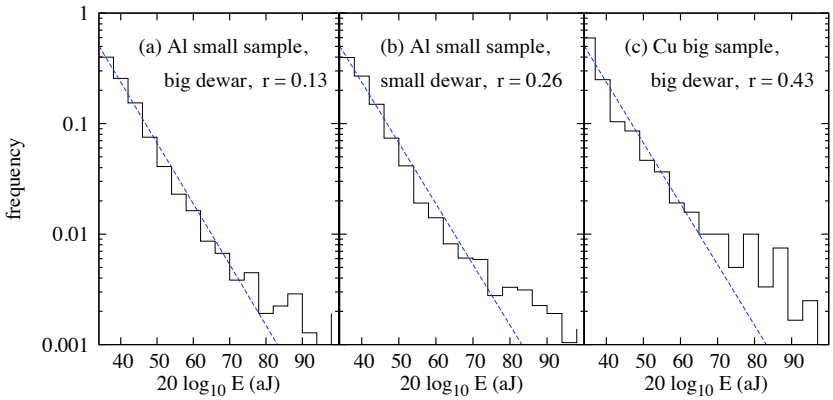

FIG. 2: Energy distributions of the AE events during the crisis regime for different conditions. The blue dashed line indicates the power law behavior with $p(E)dE \propto E^{-2.1}dE$. The ratio between the diameters of the sample and the dewar, $r = d_s/d_d$, is indicated in each case. We opted to show in the paper the energy distribution of the case with the lowest r to minimize possible boundary effects, that would affect large energy AE events.

To describe slower conductive steps we need to use the slow time $\bar{\tau} = \bar{t}/\mathbf{Pe}$ and solve

$$\frac{\partial \bar{T}}{\partial \bar{\tau}} + \frac{\partial \bar{\xi}}{\partial \bar{\tau}} = \Delta \bar{T}. \tag{4}$$

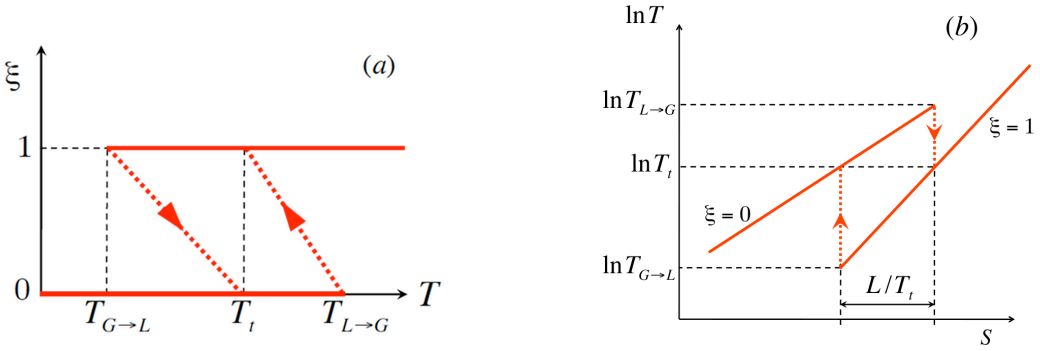

FIG. 3: (a) Phase function ξ is a hysteretic function of temperature T. (b) Schematic representation of the adiabatic phase transition in the thermodynamic $\ln T - S$ diagram, where T is the temperature and S is the entropy.

To maximally simplify the description we assumed that ξ is a spin field taking values $\xi = 0$ in the liquid phase and $\xi = 1$ in the gas phase. We also assumed that the kinetics of the phase transition is instantaneous (spin flip) and that the spin field ξ is enslaved to the field T through a hysteretic, threshold-based relation. The origin of the hysteresis is an assumption that the transformation always takes place at the fast time scale and is therefore adiabatic. In dimensional variables this means that the jump of the phase field $[\xi] = \pm 1$ is related to the jump of temperature $[T]$ by the relation $\rho c[T] + \rho L[\xi] = 0$: the (adiabatic) transition from liquid to gas is associated with a drop of temperature, while similar transition from gas to liquid leads to an increase of temperature (see Fig.3).

The complex hydrodynamical flow structure is schematically represented by the following assumptions. The spatial domain is discretized as a cubic lattice of equal 3D cells equipped with a spin variable and a discrete temperature field. We assume that the gas particles move along y direction with dimensional velocity v. During the advance the spin value is preserved $d\bar{\xi}/dt = 0$ and therefore the temperature is also preserved $d\bar{T}/dt = 0$. In the course of the advance some gas particles will overlap with fluid particles while some others will vacate lattice spots forming

'voids'. The overlapped fluid fills the voids while acquiring the average temperature of the neighboring liquid cells. During the slow conductive stages we solve a discrete version of (4) where instantaneous phase transition plays a role of either a sink (of temperature) when liquid (adiabatically) transforms into gas or a source when gas transforms into liquid. To describe heat conductivity process in different phases we use the corresponding specific heat, density and heat conductivity values. All physical quantities (heat flux, gas statistics, etc.) are averaged over typically 10^5 time steps once equilibrium steady state has been reached (with additional averaging over different realizations of the disorder).

The calculation of the dry spot size statistics is carried out in the following way. At a given time step the spatial distribution of the gas particles in the layer in contact with the metal is analyzed. A dry spot is strictly defined as the region occupied by gas meaning that each gas cell has a nearest neighbor gas cell. The dry spot size s is then the resulting 2D area. It is calculated as the number of the cells belonging to the same dry spot multiplied by the area of a unit cell a^2. The distribution of dry spot sizes is averaged over different time steps (sufficiently large to avoid overlaps) and over different realizations of the disorder.

IV. DRY SPOT SIZE DISTRIBUTIONS: ANALYSIS AND EXPONENT ESTIMATION

According to the well known subcritical-critical-supercritical behavior typically observed in systems exhibiting criticality [7] the distribution of clusters sizes is an exponentially damped power law in the subcritical regime and exhibits a peak at system sizes in the supercritical regime. If we tune an external parameter, at some intermediate point, the system reaches the critical point and the distribution becomes a true power law with a certain exponent. The observed peak in the supercritical regime is a finite size effect coming usually from spanning clusters and it is shifted to higher values of the cluster size when the system size is increased. In the thermodynamic limit it becomes a delta function placed at infinity. Here we do not talk about systems with characteristic events, like earthquakes, which may be only close to criticality due to inertia and other similar effects.

The appropriate interpretation of various finite size effects in critical systems is still a challenge in the field. One approach to this problem has been developed in the case of the Random Field Ising Model [8]. It was shown that in the critical point one can identify for finite systems different kinds of spanning clusters: some of them are truly critical and some others are artificially supercritical. Clearly, the latter have to be excluded from the distribution to obtain a faithful representation of the critical regime. Close to thermodynamic limit the truly critical clusters do not contribute considerably to the distribution comparing to the nonspanning clusters, and hence the limiting distribution is not affected by their presence or their absence. However, this is not the case in a finite size system where a peak can survive, even when artificially supercritical spanning clusters are suppressed.

As explained in [8] (see also [9]), the truly critical spanning clusters are those which are fractal. Instead, the nonfractal spanning clusters, i.e. massive spanning clusters, are supercritical. The quantitatively separation of these effects requires finite-size scaling and will be performed in a longer paper. Similar finite size effects have been previously studied in many other models including Ising's, sandpiles, tetris model, forest fire model, percolation, [10] etc.

In our 2D representation of the hot surface the avalanches/clusters can span the lattice either in 1D or 2D. In the one hand, the truly critical (fractal) spanning clusters can be either 1D- or 2D-spanning. On the other hand, the supercritical (massive) spanning clusters can only be 2D-spanning. Moreover, the probability to find a 2D-spanning cluster with fractal properties is negligible therefore all 2D-spanning clusters can be considered supercritical.

In order to be critical the distribution in a finite system must show a size interval with power law behavior even when all spanning clusters are included. The standard method to determine whether a given distribution is a power law is based on two mathematical tools: the Maximum Likelihood (ML) fit and the Kolmogorov-Smirnov (KS) distance. A detailed explanation is given in [11]. The method used in the paper is a modification of the former, which includes a special treatment of an upper cutoff proposed in [12]. This treatment opens a possibility of excluding the corrupted tail and obtaining a more accurate value for the exponent (provided that the remaining size interval contains few decades at least!).

Below we present a detailed description of our avalanche distributions. Figure 4 shows the distribution of

nonspanning dry spots sizes s with logarithmic scale and linear binning. In agreement with the theory mentioned above, the distribution clearly shows the subcritical-critical-supercritical behavior, i.e. for $\Delta T/T_t < 0.27$ the distribution shows an exponentially damped tail, at $\Delta T/T_t \simeq 0.27$ it is a power law and at $\Delta T/T_t > 0.27$ it drops again but shows a peak at large s.

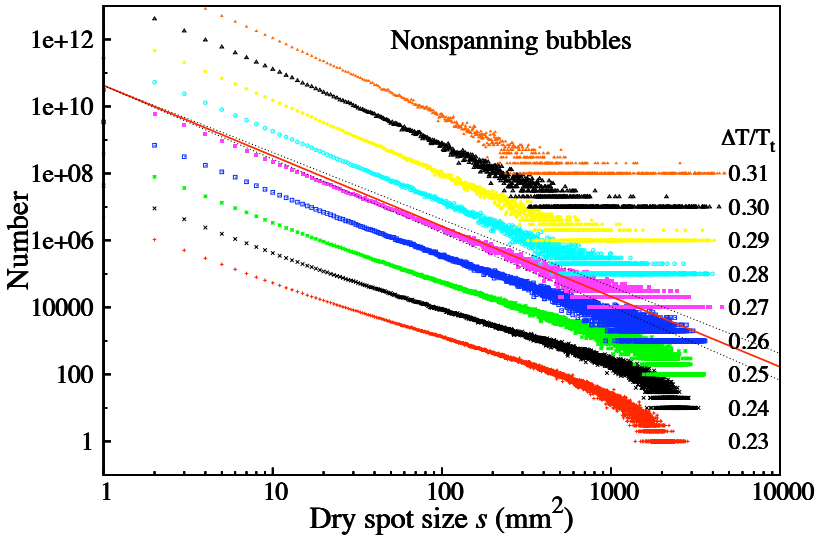

FIG. 4: Distributions of nonspanning dry spots sizes s for different temperatures. Red straight line goes as $\sim s^{-2.1}$ and black dotted lines go as $\sim s^{2.1\pm0.1}$. Logarithmic scale and linear binning are used. Curves have been vertically shifted for clarity.

Figure 5 shows individual contributions from non-spanning, 1D-spanning and 2D-spanning avalanches at different temperatures, ranging from subcritical to supercritical ones. On can see that non-spanning avalanches extend to larger sizes for $\Delta T/T_t = 0.27$, anticipating the results calculated by ML fit and KS distance.

Finally, for a better comparison with the figure presented in the manuscript, we show in Fig. 6 the distributions with logarithmic binning at three different temperatures for (a) nonspanning, (b), nonspanning plus 1D-spanning and (c) all avalanches. The distributions of the type shown in Fig. 6(b) have been analyzed for many temperatures and sizes intervals (by considering upper and lower cutoffs) and the best power-law fit is found at $\Delta T/T_t = 0.27$ with an exponent $\tau = 2.1 \pm 0.1$ for an interval of sizes about $20 - 2000\text{mm}^2$.

To illustrate this method, in Fig, 7 we compare the ML power law exponent at different temperatures and for many different sizes ranges. For instance, dotted black curve shows the ML exponent corresponding to the size range $10 - 100\text{mm}^2$. It can be seen that all curves converge for the temperature $\Delta T/T_t = 0.27$, i.e. the corresponding exponent is practically independent of the size range (with the value $\tau \simeq 2.1$). One can see that for any other temperature the value of the exponent significantly depends on the particular size range analyzed. The error of the exponent is taken to be the difference between the highest and the lowest values of the fitted exponent for $\Delta T/T_t \simeq 0.27$.

[1] S.S. Kutateladze, Kotloturbostoenie 3:10 (1948).
[2] N. Zuber, ASME J. Heat Transfer **80**, 711 (1958).
[3] I. I. Gogonin, S. S. Kutateladze, J. Eng. Phys. **33**, 1286 (1977).
[4] J. H. Lienhard, V. K. Dhir, NASA CR-2270 (1973).
[5] Alluminium alloy 2030 in: Thermophysical Properties, Division of National Institute of Standards and Technology.
[6] See URL: http://webbook.nist.gov/cgi/cbook.cgi?ID=C7727379.
[7] See, for instance, J. P. Sethna *et al.*, Phys. Rev. Lett. **70** 3347, (1993), J. P. Sethna, K. A. Dahmen and C. R. Myers, Nature **410**, 242 (2001), O. Kinouchi and M. Copelli, Nature Phys. **2**, 348 (2006), A. Corral, C. J. Pérez and A. Díaz-Guilera,

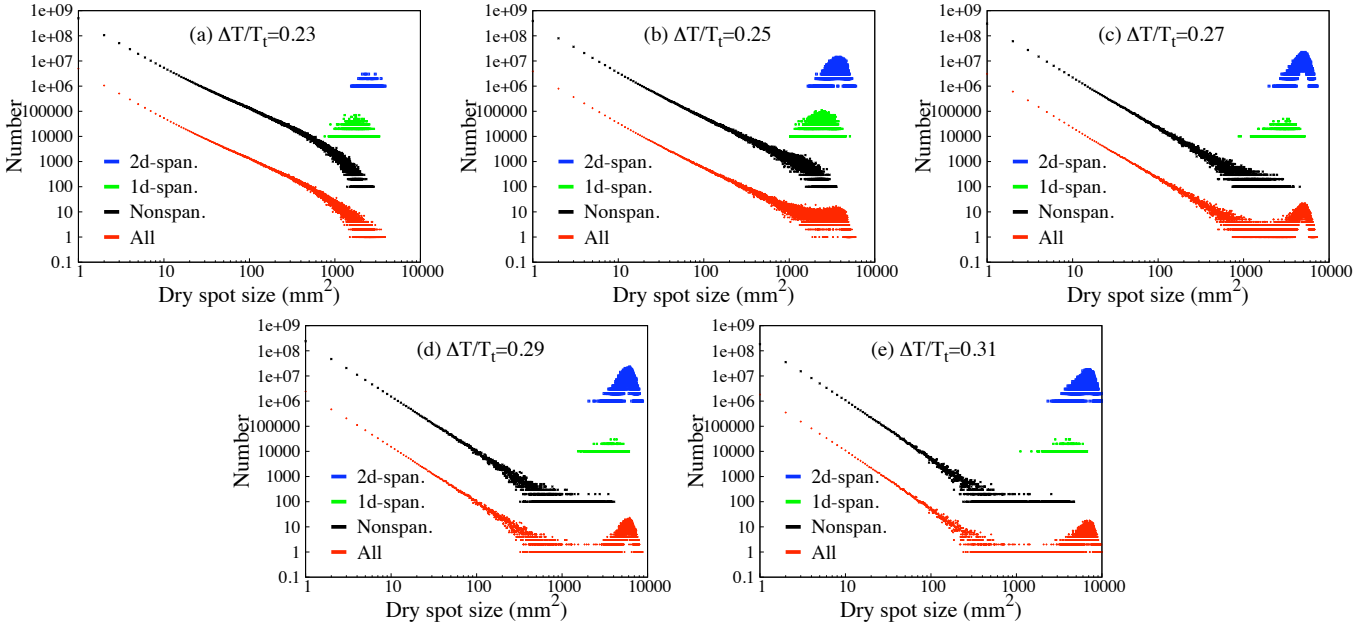

FIG. 5: (a)-(e) Distributions of the different contributions of dry spots (2D-spanning, 1D-spanning and nonspanning) for different temperatures. Logarithmic scale and linear binning are used. Curves have been vertically shifted for clarity.

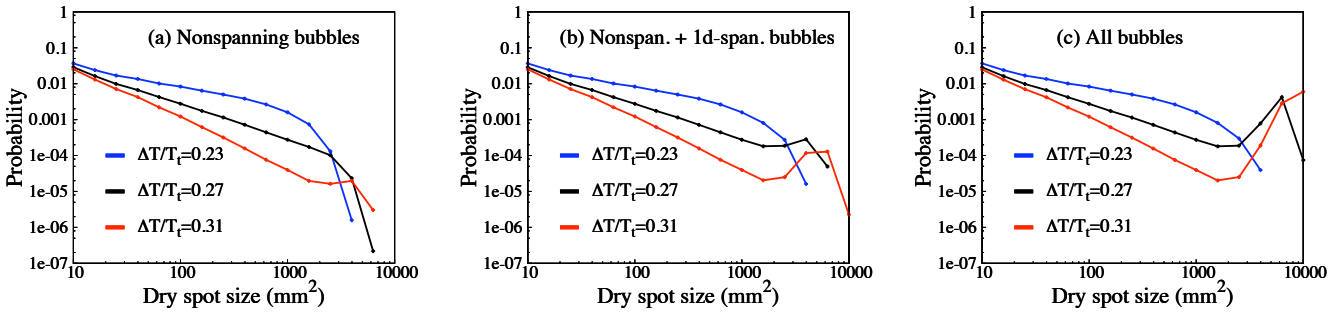

FIG. 6: Distributions of dry spot sizes at three different temperatures for (a) nonspanning, (b), nonspanning plus 1D-spanning and (c) all dry spots. Logarithmic scale and logarithmic binning are used.

Phys. Rev. Lett. **78**, 1492 (1997), L. Gil and D. Sornette, Phys. Rev. Lett. **76**, 3991 (1996), E. Vives and A. Planes, Phys. Rev. B **63**, 134431 (2001), A. Tejedor, J. B. Gómez and A. F. Pacheco, Phys. Rev. E **79**, 046102 (2009), etc.

[8] F. J. Pérez-Reche and Vives, Phys. Rev. B **67**, 134421 (2003).

[9] Y. Shim, L.E. Levine and R. Thomson, Phys. Rev. E **65**, 046146 (2002).

[10] See, for instance, P. Bak, C. Tang and K. Wiesenfeld, Phys. Rev. Lett. **59**, 381 (1987), S. Krishnamurthy, V. Loreto and S. Roux, Phys. Rev. Lett. **84**, 1039 (2000), F. J. Pérez-Reche, L. Truskinovsky and G. Zanzotto, Phys. Rev. Lett. **101**, 230601 (2008), S. Clar *et al.*, Phys. Rev. E **56**, 2467 (1997), J. M. González, O. A. Chubykalo and J. González, Phys. Rev. B **55**, 921 (1997), etc. For reviews, see, for instance, D. L. Turcotte, Rep. Prog. Phys. **62** 1377 (1999) and J. A. Bonachela and M. A. Muñoz, J. Stat. Mech. P09009 (2009).

[11] A. Clauset *et al.*, SIAM review **51**, 661 (2009).

[12] O. Peters *et al.*, J. Stat. Mech., P1103 (2010) and J. Baró and E. Vives, arXiv:1202.2043v2 [cond-mat.stat-mech].

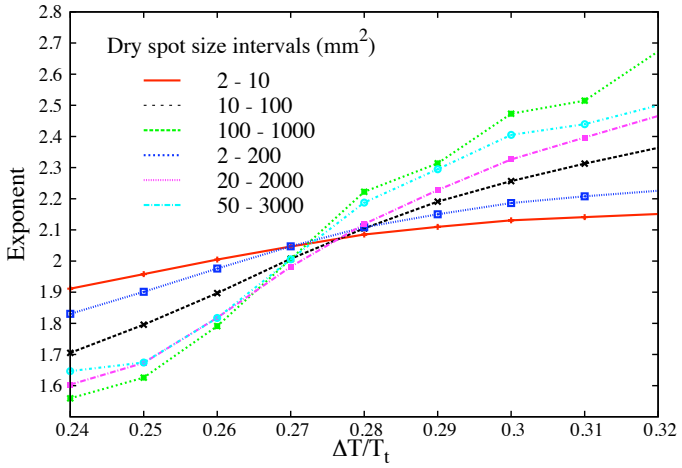

FIG. 7: Exponent found by Maximum Likelihood fit for different dry spot size ranges and for different temperatures. The value of the exponent is independent of the size interval around $\Delta T/T_t = 0.27$, and the corresponding value is approximately $\tau \sim 2.1$.